Supplementary Material for "Theory of spin-polarized scanning tunneling microscopy with topological insulator tips'

Zhuo-Yuan Shi,[1] Chuang Li,[1,*] Lin Jiao,[1,†] Huiqiu Yuan,[1] Zhenyu Wang,[2,3] Xianhui Chen,[2,3] and Lun-Hui Hu[1,‡]

[1] *Center for Correlated Matter and School of Physics, Zhejiang University, Hangzhou 310058, China*
[2] *Department of Physics, University of Science and Technology of China, Hefei, Anhui, China*
[3] *Hefei National Laboratory, University of Science and Technology of China, Hefei, 230088, China*

CONTENTS

S1. Spin-resolved Landauer-Büttiker formalism 1
A. Retarded Green function and terminal self-energies 1
B. Linear-response Büttiker equations and probe voltages 3
1. Normal dephasing 4
2. Spin dephasing 5
3. Bardeen-type and Büttiker-probe-mediated contributions 6
C. Lattice Hamiltonian and ribbon geometry 7
D. Reversal of helical chirality 7
E. Local current from the lattice continuity equation 9

S2. Dependence on contact geometry, dephasing strength, and tip–sample coupling 11
A. Contact-length and dephasing-strength dependence 11
B. Dependence on the tip–sample coupling strength 12

S3. Magnetization-dependent conductance and bias-induced contrast reversal 12

S4. Rashba spin–orbit coupling and the calculation of main text Fig. 5 12
A. Rashba Hamiltonian and terminal conventions 12
B. Nonequilibrium density matrix approach and consistency with the main text 13
C. Mode-resolved coherent scattering states and local spin polarization 14
1. Incoming Bloch mode and unit-flux normalization 14
2. Residual of the incoming wave on the cut left lead 14
3. Outgoing corrections and elimination of the two leads 15
4. Finite linear solve and numerical conventions 16
D. Local spin polarization of a single scattering state 16

References 16

S1. SPIN-RESOLVED LANDAUER-BÜTTIKER FORMALISM

A. Retarded Green function and terminal self-energies

The schematic of the full Hamiltonian system is shown in Fig. S1. We first consider the system with spin-σ_z conservation, so that we can label the index $i = (\alpha, \sigma)$ as a composite terminal-spin index, where $\alpha \in \{L, R, 1, \ldots, N\}$ and $\sigma = \uparrow, \downarrow$. Here, L refers to the left semi-infinite quantum spin Hall (QSH) insulator, R represents the right semi-infinite spin-degenerate normal metal (NM), and N is the total number of selected sites on the QSH tip where Büttiker probes are attached. The transmission $T_{i\leftarrow j}$ from terminal j to terminal i is calculated within the central scattering region (length $L_{\mathrm{QSH}} + L_{\mathrm{NM}}$, width N_y), as illustrated in Fig. S1.

* lichuang.zju@outlook.com
† lin.jiao@zju.edu.cn
‡ lunhui@zju.edu.cn

In the main text, we employ a QSH tip as a concrete example to evaluate the tunneling spin polarization. While the Hamiltonians for the QSH tip, the normal metal, and their contact are provided in the main text, the full Hamiltonian of the central scattering region H_C is illustrated in Fig. S1.

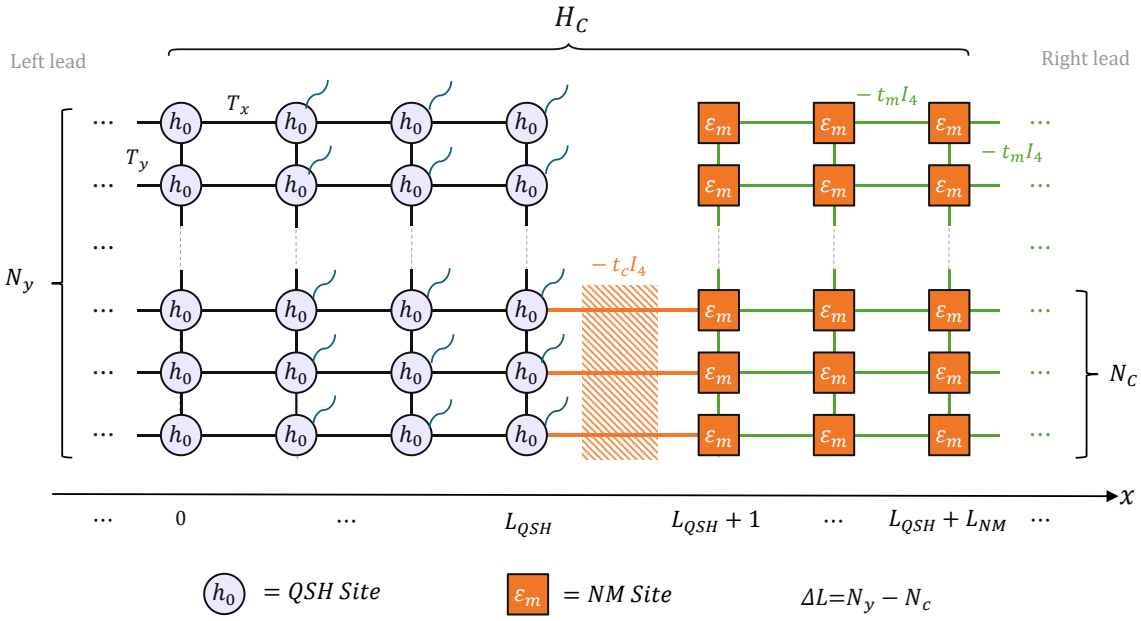

FIG. S1. Illustration of the system.

The retarded Green's function of the central scattering region is given by

$$G^r(E) = \left[(E+i0^+)\mathbf{I} - H_C - \Sigma_L^r(E) - \Sigma_R^r(E) - \sum_{p,\sigma}\Sigma_{p\sigma}^r\right]^{-1}, \tag{S1}$$

where $G^r(E)$ is a $4S \times 4S$ matrix, with $S = (L_{\mathrm{QSH}} + L_{\mathrm{NM}}) \times N_y$ being the number of spatial sites in the central region. The factor of 4 accounts for the 2 orbitals and 2 spins per site, and the advanced Green's function is $G^a(E) = [G^r(E)]^\dagger$. The central-region Hamiltonian H_C is illustrated in Fig. S2, where the contact hopping amplitude t_c (defined within H_{contact}) determines whether the geometry is a symmetric or asymmetric contact.

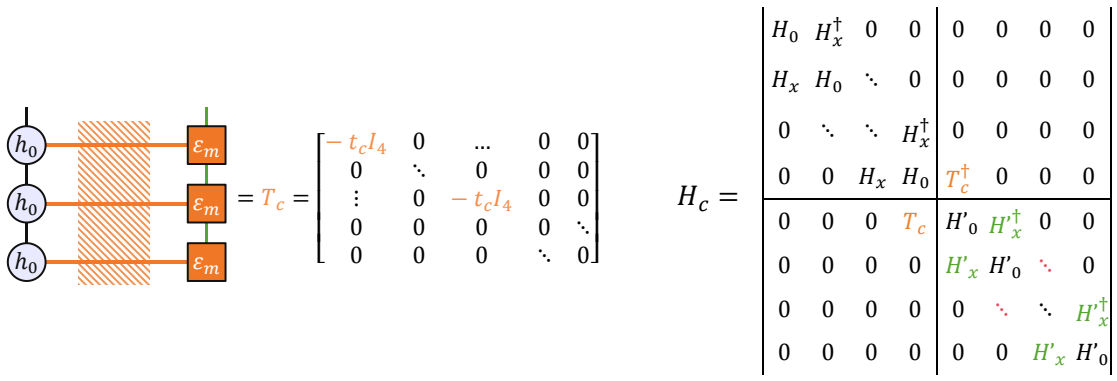

FIG. S2. Illustration of the Hamiltonian components for the entire central scattering region, including the tip-sample contact. H_0, H_x, H'_0, and H'_x are illustrated in Fig. S3.

In Eq. (S1), the left semi-infinite QSH lead and the right semi-infinite NM lead contribute to the self-energies, which

are given by

$$\Sigma_L^r(E) = \begin{bmatrix} H_x g_L^r(E) H_x^\dagger & \cdots & 0 \\ \vdots & \ddots & \vdots \\ 0 & \cdots & 0 \end{bmatrix}, \quad \Sigma_R^r(E) = \begin{bmatrix} 0 & \cdots & 0 \\ \vdots & \ddots & \vdots \\ 0 & \cdots & H'^\dagger_x g_R^r(E) H'_x \end{bmatrix}. \tag{S2}$$

Here, the left self-energy $\Sigma_L^r(E)$ has the same dimension as H_C and is nonzero only in the subspace corresponding to the $x = 0$ slice, with dimensions $4N_y \times 4N_y$. Similarly, the right self-energy $\Sigma_R^r(E)$ also shares the dimension of H_C but is nonzero only in the slice at $x = L_{\mathrm{QSH}} + L_{\mathrm{NM}}$. Moreover, $g_L^r(E)$ is the surface Green's function of the left lead, where H_{QSH} is the Hamiltonian of the semi-infinite lead occupying the region $x \leq -1$. Likewise, $g_R^r(E)$ is the surface Green's function of the right lead. H_0 and H_x, defined in Fig. S3, are the intra-slice Hamiltonian and the inter-slice hopping matrix in the QSH lead, respectively. Similarly, H'_0 and H'_x are the intra-slice Hamiltonian and the inter-slice hopping matrix in the NM lead.

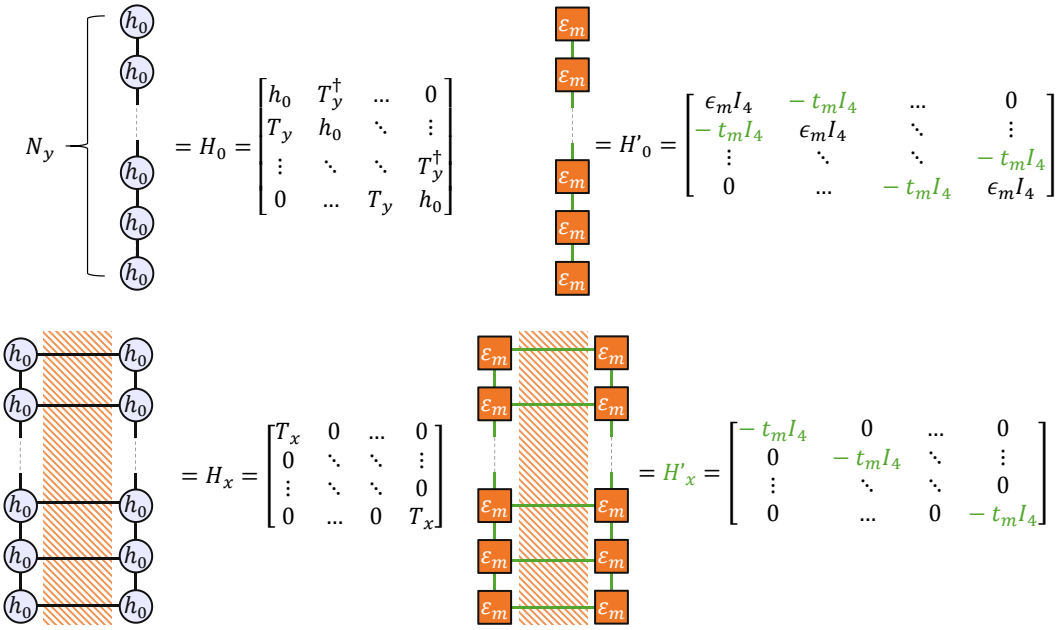

FIG. S3. Illustration of the Hamiltonian for H_0, H_x, H'_0, and H'_x.

Moreover, in Eq. (S1), the self-energies introduced by the Büttiker probes are given by

$$\Sigma_{p\sigma}^r = -\frac{i\beta}{2}\Pi_{p\sigma}, \tag{S3}$$

where $\Pi_{p\sigma}$ projects onto all orbitals of spin σ at site p (i.e., the spin-σ block of the on-site Hilbert space). The spin-independent probe (dephasing) strength $\beta \geq 0$ determines the broadening of this local self-energy.

The transmission coefficients $T_{i\leftarrow j}$ from terminal j to terminal i are evaluated using the Caroli formula,

$$T_{i\leftarrow j}(E) = \mathrm{Tr}[\Gamma_i G^r(E) \Gamma_j G^a(E)], \tag{S4}$$

where the trace runs over the spatial and orbital degrees of freedom within the central region. The broadening matrices for the left lead, right lead, and local probes are respectively given by $\Gamma_L = i(\Sigma_L^r - \Sigma_L^a)$, $\Gamma_R = i(\Sigma_R^r - \Sigma_R^a)$, and $\Gamma_{p\sigma} = i(\Sigma_{p\sigma}^r - \Sigma_{p\sigma}^a) = \beta\Pi_{p\sigma}$, with the advanced self-energy defined as $\Sigma^a = (\Sigma^r)^\dagger$. Because the composite index i incorporates the spin degree of freedom, this framework is termed the spin-resolved Landauer-Büttiker formalism.

B. Linear-response Büttiker equations and probe voltages

We now derive the self-consistent probe voltages used in the transport calculations. The corresponding spin-resolved transmissions are denoted as $T_{\alpha\sigma\leftarrow p\sigma'}$ or $T_{p\sigma\leftarrow q\sigma'}$, all evaluated at a fixed energy E. The chemical potential of terminal

i is $\mu_i = E_F + eV_i$, where $e > 0$ is the elementary charge and V_i is the terminal voltage. The two spin components of each physical lead share its voltage, $V_{L\uparrow} = V_{L\downarrow} = V_L$ and $V_{R\uparrow} = V_{R\downarrow} = V_R$. Consequently, the occupation function of terminal i is $f_i(E) = f(E - eV_i)$, where $f(E)$ is the equilibrium Fermi function at the common chemical potential E_F. Within the Landauer-Büttiker formalism, the current entering terminal i is given by

$$I_i = \frac{e}{h} \int dE \sum_{j \neq i} \left[T_{i \leftarrow j}(E) f_j(E) - T_{j \leftarrow i}(E) f_i(E) \right]. \tag{S5}$$

The first term represents electrons entering terminal i from the other terminals, whereas the second represents electrons emitted from terminal i into the other terminals. For a current-conserving multiterminal system, the unitarity of the scattering matrix requires that the total transmission into each terminal equals the total transmission out of it,

$$\sum_{j \neq i} T_{i \leftarrow j}(E) = \sum_{j \neq i} T_{j \leftarrow i}(E). \tag{S6}$$

This transmission-balance relation ensures that Eq. (S5) yields zero current in every terminal when all reservoirs share the same Fermi distribution. To obtain the linear-response equations, we expand the terminal distributions around the common equilibrium chemical potential E_F. To first order in the applied voltages, since $f(E - eV_i) = f(E) - eV_i\, \partial_E f(E) + O(V_i^2)$, we obtain

$$I_i = \frac{e^2}{h} \int dE \left[-\partial_E f(E) \right] \sum_{j \neq i} \left[T_{i \leftarrow j}(E) V_j - T_{j \leftarrow i}(E) V_i \right] + O(V^2). \tag{S7}$$

The equilibrium contribution vanishes identically owing to the balance relation in Eq. (S6). At zero temperature, $-\partial_E f(E) \to \delta(E - E_F)$, and the energy integral reduces to

$$I_i = \frac{e^2}{h} \sum_{j \neq i} \left[T_{i \leftarrow j}(E_F) V_j - T_{j \leftarrow i}(E_F) V_i \right]. \tag{S8}$$

By evaluating the transmissions at a specific incident energy E (i.e., setting $E_F = E$ for an energy-resolved calculation), this expression exactly reproduces the multiterminal Büttiker equation, Eq. (3) of the main text.

For convenience, we express the linear-response equations in matrix form,

$$I_i = \frac{e^2}{h} \sum_j C_{ij} V_j, \qquad C_{ij} = \begin{cases} T_{i \leftarrow j}, & i \neq j, \\ -\displaystyle\sum_{k \neq i} T_{k \leftarrow i}, & i = j. \end{cases} \tag{S9}$$

Here, C_{ij} is a dimensionless matrix constructed entirely from the transmission coefficients at the chosen energy. Its diagonal element is minus the total transmission leaving terminal i, while each off-diagonal element represents the transmission from terminal j into terminal i. The physical-lead voltages are specified externally, whereas the probe voltages are determined by imposing the corresponding zero-current conditions. We now describe the two specific probe conditions used in the main text.

1. *Normal dephasing*

We first consider normal (spin-conserving) dephasing, where each spin channel of the probe acts as an independent floating terminal with a vanishing net current:

$$I_{p\uparrow} = I_{p\downarrow} = 0, \qquad p = 1, \ldots, N. \tag{S10}$$

We group the unknown probe voltages into a $2N$-component vector,

$$\boldsymbol{V}_P = \begin{pmatrix} V_{1\uparrow} & V_{1\downarrow} & \cdots & V_{N\uparrow} & V_{N\downarrow} \end{pmatrix}^T. \tag{S11}$$

Similarly, the externally applied voltages at the physical leads form the vector $\boldsymbol{V}_{LR} = (V_{L\uparrow}, V_{L\downarrow}, V_{R\uparrow}, V_{R\downarrow})^{\mathsf{T}}$. Owing to the independent current constraints ($I_{p\sigma} = 0$), the two spin channels of a given Büttiker probe can generally acquire different floating voltages (i.e., $V_{p\uparrow} \neq V_{p\downarrow}$).

For an individual probe spin channel (p,σ), the zero-current condition obtained from Eq. (S9) is

$$V_{p\sigma}\sum_{j\neq(p,\sigma)}T_{j\leftarrow p\sigma}-\sum_{q,\sigma'(q,\sigma')\neq(p,\sigma)}T_{p\sigma\leftarrow q\sigma'}V_{q\sigma'}=\sum_{\beta=L,R}\sum_{\sigma'}T_{p\sigma\leftarrow\beta\sigma'}V_{\beta\sigma'}. \tag{S12}$$

Here the first sum includes all spin-resolved physical leads and Büttiker probes other than (p,σ), whereas the second sum includes only the other spin-resolved Büttiker probes. Collecting the $2N$ probe equations gives the matrix equation

$$C_{PP}\boldsymbol{V}_P=-C_{P,LR}\boldsymbol{V}_{LR}. \tag{S13}$$

The matrix C_{PP} has dimension $2N\times 2N$, and its elements are

$$[C_{PP}]_{p\sigma,q\sigma'}=C_{p\sigma,q\sigma'}. \tag{S14}$$

The matrix $C_{P,LR}$ has dimension $2N\times 4$, with elements

$$[C_{P,LR}]_{p\sigma,\beta\sigma'}=C_{p\sigma,\beta\sigma'},\qquad \beta=L,R. \tag{S15}$$

Thus C_{PP} describes the transmission couplings among the floating spin-resolved Büttiker probes, while $C_{P,LR}$ describes their coupling to the externally biased physical leads. The self-consistent probe voltages are obtained by solving

$$\boldsymbol{V}_P=-C_{PP}^{-1}C_{P,LR}\boldsymbol{V}_{LR}. \tag{S16}$$

When the Hamiltonian conserves σ_z, all transmissions between opposite spin sectors vanish.

2. Spin dephasing

For spin dephasing, the two spin channels at each probe site share a common floating voltage,

$$V_{p\uparrow}=V_{p\downarrow}=V_p, \tag{S17}$$

and only their total charge current is required to vanish:

$$I_{p\uparrow}+I_{p\downarrow}=0. \tag{S18}$$

Unlike normal dephasing, the currents in the two spin channels, $I_{p\uparrow}$ and $I_{p\downarrow}$, are not required to vanish individually; they can be finite and opposite ($I_{p\uparrow}+I_{p\downarrow}=0$). In the absence of spin-orbit coupling, this allows the probe to absorb an electron from one spin channel and reinject it into the other, effectively mediating spin-flip backscattering. Consequently, the probe voltages to be determined now form an N-component vector,

$$\boldsymbol{V}_P^{spin}=\begin{pmatrix}V_1 & V_2 & \cdots & V_N\end{pmatrix}^T, \tag{S19}$$

while the physical voltage vector remains $\boldsymbol{V}_{LR}^{spin}=(V_L,V_R)^T$. To derive the corresponding matrix equation, we sum the two current rows associated with $(p,\uparrow)$ and $(p,\downarrow)$ in Eq. (S9), after imposing the common voltage V_p. Contributions describing transmission between the two spin channels of the same probe cancel because they connect channels held at the same voltage. The resulting charge-balance equation is

$$V_p\left[\sum_{\beta=L,R}\sum_{\sigma,\sigma'}T_{\beta\sigma'\leftarrow p\sigma}+\sum_{q\neq p}\sum_{\sigma,\sigma'}T_{q\sigma'\leftarrow p\sigma}\right]\quad-\sum_{q\neq p}V_q\sum_{\sigma,\sigma'}T_{p\sigma\leftarrow q\sigma'}=\sum_{\beta=L,R}V_\beta\sum_{\sigma,\sigma'}T_{p\sigma\leftarrow\beta\sigma'}. \tag{S20}$$

As in the normal-dephasing case, the N charge-balance equations can be written in matrix form,

$$C_{PP}^{\mathrm{spin}}\boldsymbol{V}_P^{spin}=-C_{P,LR}^{\mathrm{spin}}\boldsymbol{V}_{LR}^{spin}. \tag{S21}$$

Here, C_{PP}^{spin} is an $N\times N$ matrix obtained by summing over the spin indices of the original C matrix,

$$[C_{PP}^{\mathrm{spin}}]_{pq}=\sum_{\sigma,\sigma'}C_{p\sigma,q\sigma'}. \tag{S22}$$

Explicitly, its off-diagonal and diagonal elements are

$$
\begin{aligned}
[C_{PP}^{\mathrm{spin}}]_{pq} &= \sum_{\sigma,\sigma'} T_{p\sigma\leftarrow q\sigma'}, \qquad p \neq q, \\
[C_{PP}^{\mathrm{spin}}]_{pp} &= -\sum_{\sigma,\sigma'} \left[\sum_{\beta=L,R} T_{\beta\sigma'\leftarrow p\sigma} + \sum_{q\neq p} T_{q\sigma'\leftarrow p\sigma} \right].
\end{aligned}
\tag{S23}
$$

The physical-lead coupling matrix $C_{P,LR}^{\mathrm{spin}}$ has dimension $N \times 2$, with elements

$$
[C_{P,LR}^{\mathrm{spin}}]_{p\beta} = \sum_{\sigma,\sigma'} C_{p\sigma,\beta\sigma'} = \sum_{\sigma,\sigma'} T_{p\sigma\leftarrow\beta\sigma'}. \tag{S24}
$$

The shared probe voltages are therefore determined by

$$
\boldsymbol{V}_P^{spin} = -(C_{PP}^{\mathrm{spin}})^{-1} C_{P,LR}^{\mathrm{spin}} \boldsymbol{V}_{LR}^{spin}. \tag{S25}
$$

Thus spin dephasing requires solving only an N-dimensional linear system, compared with the $2N$-dimensional system for normal dephasing [3–5].

3. Bardeen-type and Büttiker-probe-mediated contributions

Once the floating probe voltages have been determined, they are substituted into the current equations of the physical leads. In matrix form, this elimination is the Schur complement of the floating-probe block,

$$
C_{LR}^{\mathrm{eff}} = C_{LR,LR} - C_{LR,P} C_{PP}^{-1} C_{P,LR}, \tag{S26}
$$

where the physical spin channels are summed into the two physical leads L and R. The block matrices refer to the corresponding normal- or spin-dephasing prescription. In the latter case, we have a similar equation:

$$
C_{LR}^{\mathrm{eff,spin}} = C_{LR,LR}^{spin} - C_{LR,P}^{spin} (C_{PP}^{spin})^{-1} C_{P,LR}^{spin}, \tag{S27}
$$

For the tunneling spin polarization, we retain the spin-resolved current collected by the right lead. Because the two physical spin channels share the voltage V_R, and because the transmission-balance relation in Eq. (S6) holds for each composite terminal–spin index, the collected current can be written as:

$$
\frac{h}{e^2} I_{R\sigma} = (V_L - V_R) \sum_{\sigma'} T_{R\sigma\leftarrow L\sigma'} + \sum_{p,\sigma'} T_{R\sigma\leftarrow p\sigma'} (V_{p\sigma'} - V_R). \tag{S28}
$$

For normal dephasing, $V_{p\uparrow}$ and $V_{p\downarrow}$ are determined independently from Eq. (S16). For spin dephasing, both are replaced by the shared voltage V_p obtained from Eq. (S25). Setting $V_L = V$ and $V_R = 0$, and dividing the collected current by e^2V/h, gives the spin-resolved effective transmission

$$
T_{R\sigma\leftarrow L}^{\mathrm{eff}}(E) = \sum_{\sigma'} T_{R\sigma\leftarrow L\sigma'}(E) + \sum_{p,\sigma'} T_{R\sigma\leftarrow p\sigma'}(E) \frac{V_{p\sigma'}}{V}. \tag{S29}
$$

This is the key equation presented in the main text. And the tunneling spin polarization is then calculated as

$$
P_s(E) = \frac{T_{R\uparrow\leftarrow L}^{\mathrm{eff}}(E) - T_{R\downarrow\leftarrow L}^{\mathrm{eff}}(E)}{T_{R\uparrow\leftarrow L}^{\mathrm{eff}}(E) + T_{R\downarrow\leftarrow L}^{\mathrm{eff}}(E)}, \tag{S30}
$$

which reproduces Eq. (5) of the main text. For the reversed transport direction, we set $V_R = V$ and $V_L = 0$, solve the corresponding floating-probe equations again, and evaluate $T_{L\sigma\leftarrow R}^{\mathrm{eff}}$ in the same laboratory spin basis. The resulting polarization is denoted by $\overline{P}_s$ in the main text.

C. Lattice Hamiltonian and ribbon geometry

To characterize the helical edge states of the QSH tip, we first consider the Bloch Hamiltonian corresponding to Eq. (7) of the main text. In the ordered basis $\{|s,\uparrow\rangle, |p_-,\uparrow\rangle, |s,\downarrow\rangle, |p_+,\downarrow\rangle\}$, it takes the form

$$H_{\mathrm{QSH}}(\boldsymbol{k}) = [M - 4t + 2t(\cos k_x + \cos k_y)]\sigma_0\tau_z - A\sin k_x\,\sigma_z\tau_x - A\sin k_y\,\sigma_0\tau_y. \tag{S31}$$

Here σ_i and τ_i act on the spin and orbital degrees of freedom, respectively. We set the lattice constant to $a = 1$. The parameter M controls the band inversion, t is the orbital-dependent hopping amplitude, and A is the interorbital hopping strength.

To implement Eq. (S31) on a square lattice, we use the Fourier convention

$$c_{\boldsymbol{r}} = N_{\mathrm{lattice}}^{-1/2}\sum_{\boldsymbol{k}} e^{i\boldsymbol{k}\cdot\boldsymbol{r}}c_{\boldsymbol{k}}, \tag{S32}$$

and define the hopping matrix by $H_{\boldsymbol{r}+\mu,\boldsymbol{r}} = T_\mu$. The Hamiltonian is then obtained from the on-site and nearest-neighbor blocks according to

$$H_{\mathrm{QSH}}(\boldsymbol{k}) = h_0 + \sum_{\mu=x,y}(T_\mu e^{-ik_\mu} + T_\mu^\dagger e^{ik_\mu}), \tag{S33}$$

where the four-by-four matrices h_0 and T_μ are given by

$$h_0 = (M - 4t)\sigma_0\tau_z, \quad T_x = t\sigma_0\tau_z - \frac{iA}{2}\sigma_z\tau_x, \quad T_y = t\sigma_0\tau_z - \frac{iA}{2}\sigma_0\tau_y. \tag{S34}$$

The hopping blocks in the opposite directions are $T_x^\dagger$ and $T_y^\dagger$. Thus the lattice Hamiltonian has exactly the real-space form given in Eq. (7) of the main text.

For the ribbon calculation, we impose open boundary conditions along y while retaining translation invariance along x. Each longitudinal slice contains N_y transverse sites with 4 internal degrees of freedom per site, yielding a total of $4N_y$ components. In the x-slice basis, the intra-slice and forward inter-slice blocks are(also defined in Fig. S3):

$$\begin{aligned}[H_0]_{yy'} &= \delta_{yy'}h_0 + \delta_{y,y'+1}T_y + \delta_{y+1,y'}T_y^\dagger,\\ [H_x]_{yy'} &= \delta_{yy'}T_x, \qquad 0 \le y, y' \le N_y - 1.\end{aligned} \tag{S35}$$

Fourier transforming only along the longitudinal direction yields the $4N_y \times 4N_y$ ribbon Hamiltonian

$$H_{\mathrm{QSH}}(k_x) = H_0 + H_x e^{-ik_x} + H_x^\dagger e^{ik_x}. \tag{S36}$$

We obtain the energy spectrum by diagonalizing Eq. (S36) at each k_x. Figs. S4(a,b) shows the spin-resolved spectra of the lower and upper boundaries, respectively, for $N_y = 50$. The color indicates the dimensionless spin expectation value $\langle s_z\rangle \equiv \langle\sigma_z\tau_0\rangle$. To verify their spatial localization, we select the representative eigenstates indicated by open circles in Figs. S4(a,b) and calculate their probability distributions,

$$P(y) = \sum_{\gamma=1}^{4}|\psi_{n,k_x;\gamma}(y)|^2, \qquad \sum_{y=0}^{N_y-1}P(y) = 1. \tag{S37}$$

Here γ runs over the four spin-orbital components of the selected eigenstate. As shown in Figs. S4(c,d), the probability is strongly concentrated near $y = 0$ for the lower-edge state and near $y = N_y - 1$ for the upper-edge state, with rapid decay into the interior.

D. Reversal of helical chirality

To further verify that the sign of the tunneling spin polarization is determined by the chirality of the helical edge states, we reverse their spin-momentum locking by changing $A \to -A$ only in the y-direction hopping T_y, while keeping T_x unchanged, as discussed in Sec. III B of the main text. The resulting momentum-space Hamiltonian reads

$$H_{\mathrm{QSH}}^{\mathrm{rev}}(\boldsymbol{k}) = [M - 4t + 2t(\cos k_x + \cos k_y)]\sigma_0\tau_z - A\sin k_x\,\sigma_z\tau_x + A\sin k_y\,\sigma_0\tau_y. \tag{S38}$$

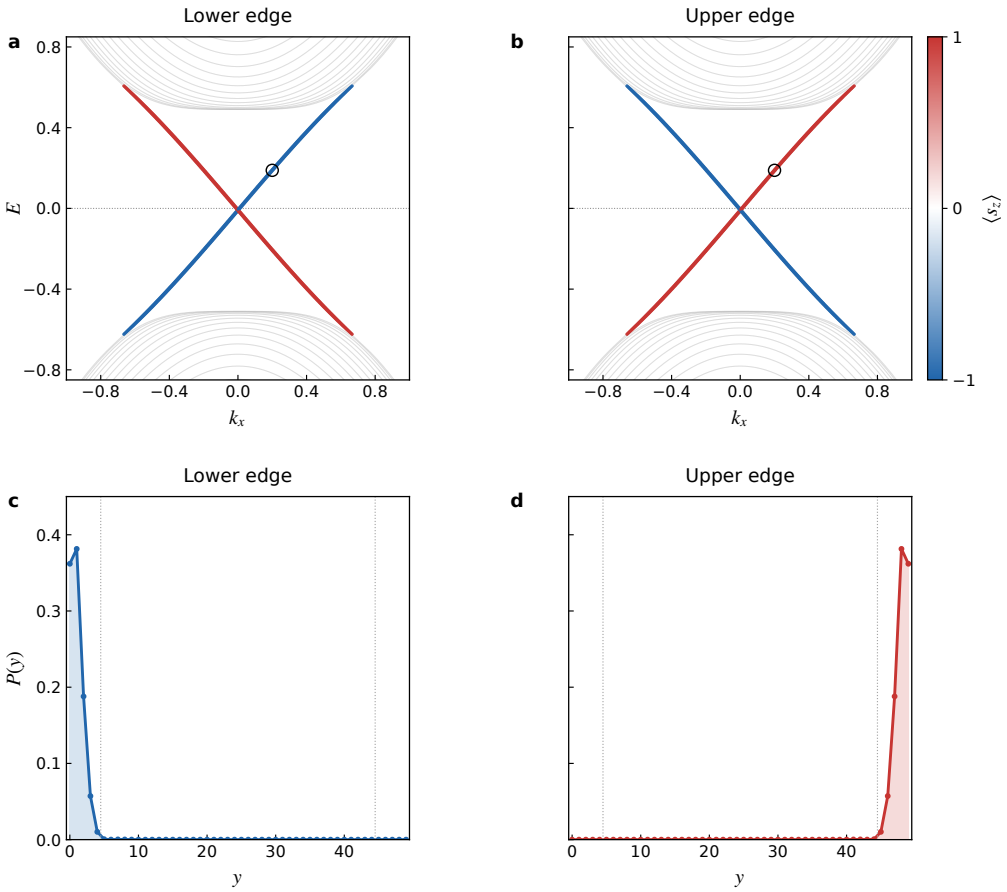

FIG. S4. Helical edge states of the QSH ribbon. (a,b) Energy spectra highlighting states localized at the lower and upper edges, respectively. Colors indicate the dimensionless spin expectation value $\langle s_z \rangle = \langle \sigma_z \tau_0 \rangle$, while gray curves show bulk-like subbands. The counterpropagating edge modes carry opposite spins, with the spin–momentum locking reversed between the two boundaries. (c,d) Normalized transverse probability distributions $P(y)$ of the states marked by open circles in (a,b), showing localization near $y = 0$ and $y = N_y - 1$, respectively, and rapid decay into the interior. The parameters are $N_y = 50$, $M = 0.5t$, and $A = t$.

Compared with the original Hamiltonian in Eq. (S31), this modification reverses the helical chirality without changing the energy spectrum. Consequently, the propagation directions associated with the spin-up and spin-down edge modes are interchanged, while the contact geometry and dephasing strength remain unchanged.

Figure S5 presents the spin-resolved transmission spectra and corresponding local current distributions for the reversed chirality. We consider four configurations: Figs. S5(a,e) a symmetric contact with spin dephasing, Figs. S5(b,f) an asymmetric contact without dephasing, Figs. S5(c,g) an asymmetric contact with normal dephasing, and Figs. S5(d,h) an asymmetric contact with spin dephasing. As in the original model, the first three configurations exhibit identical spin-resolved transmissions, resulting in vanishing tunneling spin polarization. In contrast, the coexistence of an asymmetric contact and spin dephasing produces unequal spin-resolved transmissions, as shown in Figs. S5(d).

The corresponding local current distributions in Figs. S5(e)–(h) further illustrate the microscopic mechanism. After reversing the chirality, the spin-up electrons propagate toward the contact along the shorter lower edge, whereas the spin-down electrons approach the contact along the longer upper edge. Spin-relaxing backscattering therefore suppresses the spin-down transmission more strongly, leading to $T^{\mathrm{eff}}_{R\uparrow\leftarrow L} > T^{\mathrm{eff}}_{R\downarrow\leftarrow L}$. For $E = 0.01t$, $\Delta L = 40$, and $\beta = 0.03t$, the resulting tunneling spin polarization is $P_s = +17.2\%$, exactly opposite to the original value $P_s = -17.2\%$ reported in Fig. 1(d) of the main text. This confirms that the sign of the tunneling spin polarization is determined by the chirality of the helical edge states, while its finite magnitude requires the combined effects of contact asymmetry and spin dephasing.

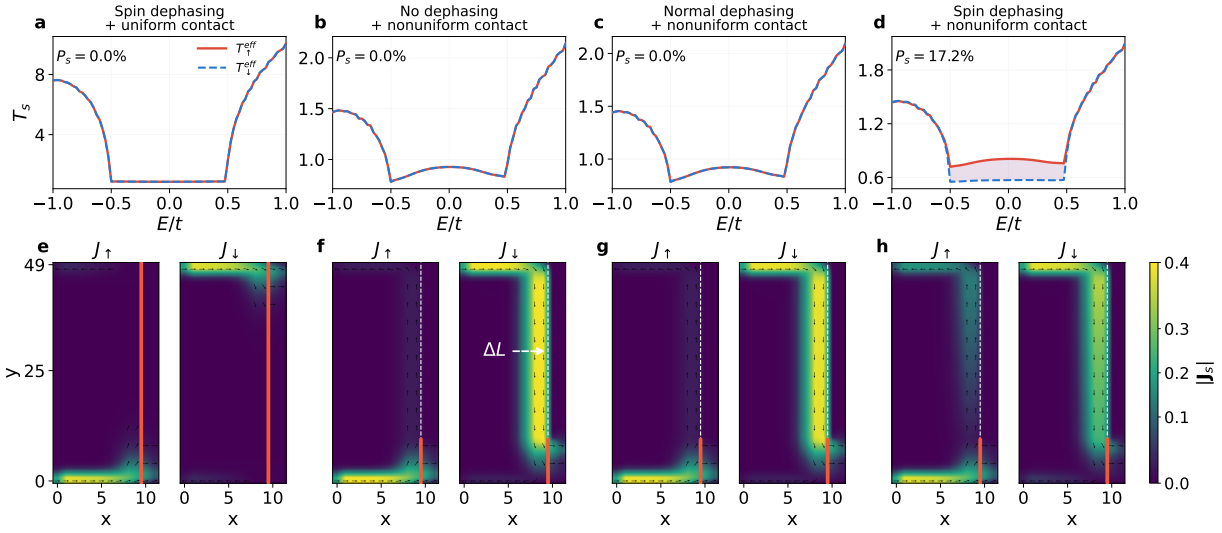

FIG. S5. Reversal of spin-selective tunneling induced by reversing the helical chirality. (a)–(d) Spin-resolved effective transmission spectra $T^{\rm eff}_{R\uparrow\leftarrow L}$ (solid red) and $T^{\rm eff}_{R\downarrow\leftarrow L}$ (dashed blue) for four configurations: (a) symmetric contact with spin dephasing, (b) asymmetric contact without dephasing, (c) asymmetric contact with normal dephasing, and (d) asymmetric contact with spin dephasing. (e)–(h) Corresponding spatial distributions of the spin-resolved local currents $J_\uparrow$ (left) and $J_\downarrow$ (right) at $E = 0.01t$. The color scale represents the local current magnitude, and the arrows indicate the current direction. Solid orange lines mark the tunneling contacts, while dashed lines indicate the noncontact regions. Reversing the helical chirality interchanges the dominant spin channel, yielding $P_s = +17.2\%$ in (d), opposite to the original result in main text Fig. 1(d).

E. Local current from the lattice continuity equation

The spatial distributions of the spin-resolved local currents in Figs. 1(e)–(h) of the main text are calculated from the lattice continuity equation using the nonequilibrium Green-function formalism [8, 9]. Since the Hamiltonian conserves σ_z in the absence of Rashba spin-orbit coupling, the local currents can be resolved into independent spin sectors. Throughout the calculation, we use the four-component basis $\{|s,\uparrow\rangle, |p_-,\uparrow\rangle, |s,\downarrow\rangle, |p_+,\downarrow\rangle\}$ defined in the main text.

Consider two neighboring lattice sites $\boldsymbol{r}$ and $\boldsymbol{r}'$, connected by the hopping block $[H_C]_{\boldsymbol{r}'\boldsymbol{r}}$. The corresponding second-quantized bond Hamiltonian is

$$\hat{H}_{\boldsymbol{r}\boldsymbol{r}'} = c^\dagger_{\boldsymbol{r}'}[H_C]_{\boldsymbol{r}'\boldsymbol{r}}c_{\boldsymbol{r}} + c^\dagger_{\boldsymbol{r}}[H_C]_{\boldsymbol{r}\boldsymbol{r}'}c_{\boldsymbol{r}'}, \tag{S39}$$

where $[H_C]_{\boldsymbol{r}\boldsymbol{r}'} = [H_C]^\dagger_{\boldsymbol{r}'\boldsymbol{r}}$. Both hopping blocks are 4×4 matrices in the spin-orbital basis. For a fixed spin σ, $c_{\boldsymbol{r}'\sigma}$ is the two-component orbital column, and the local number operator is $\hat{n}_{\boldsymbol{r}'\sigma} = c^\dagger_{\boldsymbol{r}'\sigma}c_{\boldsymbol{r}'\sigma}$. Its time evolution follows from the Heisenberg equation,

$$\frac{d\hat{n}_{\boldsymbol{r}'\sigma}}{dt} = \frac{i}{\hbar}[\hat{H}_C, \hat{n}_{\boldsymbol{r}'\sigma}]. \tag{S40}$$

The two hopping terms in Eq. (S39) contribute with opposite signs to the commutator. Using the fermionic anticommutation relations and the Hermiticity of the hopping matrix, the particle influx from $\boldsymbol{r}$ to $\boldsymbol{r}'$ becomes

$$\left.\frac{d\langle\hat{n}_{\boldsymbol{r}'\sigma}\rangle}{dt}\right|_{\boldsymbol{r}} = \frac{2}{\hbar}\,\mathrm{Im}\left\langle c^\dagger_{\boldsymbol{r}'\sigma}[H_C]^\sigma_{\boldsymbol{r}'\boldsymbol{r}}c_{\boldsymbol{r}\sigma}\right\rangle. \tag{S41}$$

To express this result in matrix form, we use the single-particle density matrix

$$\rho_{mn} = \langle c^\dagger_n c_m\rangle, \tag{S42}$$

where m and n denote complete site and internal-state indices; these indices are distinct from the terminal indices used in the transport equations. The expectation value in Eq. (S41) is then exactly the corresponding spin-diagonal element of the orbital partial trace,

$$\left\langle c^\dagger_{\boldsymbol{r}'\sigma}[H_C]^\sigma_{\boldsymbol{r}'\boldsymbol{r}}c_{\boldsymbol{r}\sigma}\right\rangle = \left[\mathrm{Tr}'\left([H_C]_{\boldsymbol{r}'\boldsymbol{r}}\rho_{\boldsymbol{r}\boldsymbol{r}'}\right)\right]_{\sigma\sigma}. \tag{S43}$$

Here Tr' retains the spin indices, as in the main text. Because the two sites are already fixed in this bond block, only the orbital indices are traced, leaving a 2×2 matrix in spin space. The density-matrix block $\rho_{\boldsymbol{r}\boldsymbol{r}'}$ contains the correlations between the creation operators at $\boldsymbol{r}'$ and the annihilation operators at $\boldsymbol{r}$.

Multiplying the particle influx by the positive elementary charge e, the spin-resolved bond current is therefore

$$J_\sigma(\boldsymbol{r} \to \boldsymbol{r}') = \frac{2e}{\hbar} \,\mathrm{Im}\left[\mathrm{Tr}'\left([H_C]_{\boldsymbol{r}'\boldsymbol{r}}\rho_{\boldsymbol{r}\boldsymbol{r}'}\right)\right]_{\sigma\sigma}. \tag{S44}$$

We next evaluate the density matrix using the lesser Green function. We choose the energy-domain normalization of the lesser Green function such that the equal-time density matrix satisfies

$$\rho = -i\int \frac{dE}{2\pi} G^<(E). \tag{S45}$$

Substituting this relation directly into Eq. (S44) gives

$$J_\sigma(\boldsymbol{r} \to \boldsymbol{r}') = -\frac{2e}{\hbar}\int \frac{dE}{2\pi} \,\mathrm{Re}\left[\mathrm{Tr}'\left([H_C]_{\boldsymbol{r}'\boldsymbol{r}}G^<_{\boldsymbol{r}\boldsymbol{r}'}(E)\right)\right]_{\sigma\sigma}. \tag{S46}$$

This is the bond-current expression in terms of the lesser Green function.

For the QSH tip connected to the physical leads and the Büttiker probes, the Keldysh equation gives

$$G^<(E) = G^r(E)\Sigma^<(E)G^a(E), \tag{S47}$$

with the lesser self-energy

$$\Sigma^<(E) = i\Big[f_L(E)\Gamma_L(E) + f_R(E)\Gamma_R(E) + \sum_{p,\sigma'} f_{p\sigma'}(E)\Gamma_{p\sigma'}(E)\Big]. \tag{S48}$$

Combining the preceding equations, we obtain

$$\rho = \int \frac{dE}{2\pi} G^r(E)\Big[f_L(E)\Gamma_L + f_R(E)\Gamma_R + \sum_{p,\sigma'} f_{p\sigma'}(E)\Gamma_{p\sigma'}\Big]G^a(E). \tag{S49}$$

Thus the two-site correlation entering the bond current is calculated directly from the same Green functions and reservoir occupations used in the multiterminal transport formalism.

To obtain the bias-induced current, we expand the reservoir occupations to linear order around the common equilibrium chemical potential E_F, using $f_i(E) = f(E) - eV_i\partial_E f(E)$. Subtracting the equilibrium contribution gives

$$\delta\rho = e\int \frac{dE}{2\pi}[-\partial_E f(E)]G^r(E) \times \Big[V_L\Gamma_L + V_R\Gamma_R + \sum_{p,\sigma'} V_{p\sigma'}\Gamma_{p\sigma'}\Big]G^a(E). \tag{S50}$$

At zero temperature, $-\partial_E f(E) = \delta(E - E_F)$. Setting $E_F = E$ for the energy-resolved calculation yields

$$\delta\rho(E) = \frac{e}{2\pi}G^r(E)\Big[V_L\Gamma_L + V_R\Gamma_R + \sum_{p,\sigma'} V_{p\sigma'}\Gamma_{p\sigma'}\Big]G^a(E). \tag{S51}$$

For the forward-bias configuration used in main text Fig. 1, we set $V_L = V$ and $V_R = 0$. Substituting Eq. (S51) into Eq. (S44), the final spin-resolved bond current is

$$J_\sigma(\boldsymbol{r} \to \boldsymbol{r}'; E) = \frac{2e^2V}{h}\,\mathrm{Im}\left[\mathrm{Tr}'\left([H_C]_{\boldsymbol{r}'\boldsymbol{r}} \times \Big[G^r(E)\Big(\Gamma_L + \sum_{p,\sigma'}\frac{V_{p\sigma'}}{V}\Gamma_{p\sigma'}\Big)G^a(E)\Big]_{\boldsymbol{r}\boldsymbol{r}'}\right)\right]_{\sigma\sigma}. \tag{S52}$$

The term proportional to Γ_L represents injection from the left lead, whereas the probe terms describe the additional reinjection required by the self-consistent zero-current conditions.

For numerical evaluation, we introduce the voltage-normalized matrix

$$\mathcal{T}_R(E) = G^r(E)\left[\Gamma_L + \sum_{p,\sigma'}\frac{V_{p\sigma'}}{V}\Gamma_{p\sigma'}\right]G^a(E). \tag{S53}$$

The bond current in units of e^2V/h consequently reduces to

$$j_\sigma(\boldsymbol{r} \to \boldsymbol{r}'; E) = 2\,\mathrm{Im}\left[\mathrm{Tr}'\left([H_C]_{\boldsymbol{r}'\boldsymbol{r}}[\mathcal{T}_R]_{\boldsymbol{r}\boldsymbol{r}'}(E)\right)\right]_{\sigma\sigma}. \tag{S54}$$

This is the expression used to evaluate the local currents in Fig. 1(e)–(h). The hopping and density-matrix blocks are 4×4 matrices in the basis of the main text. Their product is reduced by Tr', and the diagonal spin elements give the corresponding spin-resolved bond currents. For the present nearest-neighbor lattice Hamiltonian, Eq. (S54) is evaluated only between directly connected neighboring sites, $\boldsymbol{r}' = \boldsymbol{r} \pm \hat{x}$ or $\boldsymbol{r} \pm \hat{y}$.

S2. DEPENDENCE ON CONTACT GEOMETRY, DEPHASING STRENGTH, AND TIP–SAMPLE COUPLING

A. Contact-length and dephasing-strength dependence

Figure S6 compares the contact-length dependence of the spin-resolved effective transmissions under normal and spin dephasing. Here increasing $\Delta L = N_y - N_c$ corresponds to shortening the contact.

For normal dephasing, the spin-up and spin-down transmissions remain equal, and the curves for different dephasing strengths nearly overlap [Fig. S6(a)]. Both transmissions remain close to unity over a broad range of contact lengths and decrease appreciably only for the shortest contacts. Consequently, the polarization remains zero throughout the scan [Fig. S6(c)].

Spin dephasing suppresses both transmissions, but their suppression becomes unequal when the contact is asymmetric [Fig. S6(b)]. The spin-up transmission decreases more strongly than the spin-down transmission, producing a negative polarization. Its magnitude initially increases with ΔL and is generally enhanced by stronger spin dephasing [Fig. S6(d)]. For $\beta = 0.2t$, the polarization reaches approximately -0.3. In contrast, the polarization vanishes for a symmetric contact, $\Delta L = 0$, or in the coherent limit, $\beta = 0$.

For the shortest contacts, the polarization magnitude decreases again. In this regime, the spin-down transmission drops more rapidly relative to the spin-up transmission, which has already become comparatively flat. The relative transmission imbalance therefore decreases, accounting for the upturn in Fig. S6(d). This behavior is physically intuitive, as the tunneling current must vanish when the contact area goes to zero.

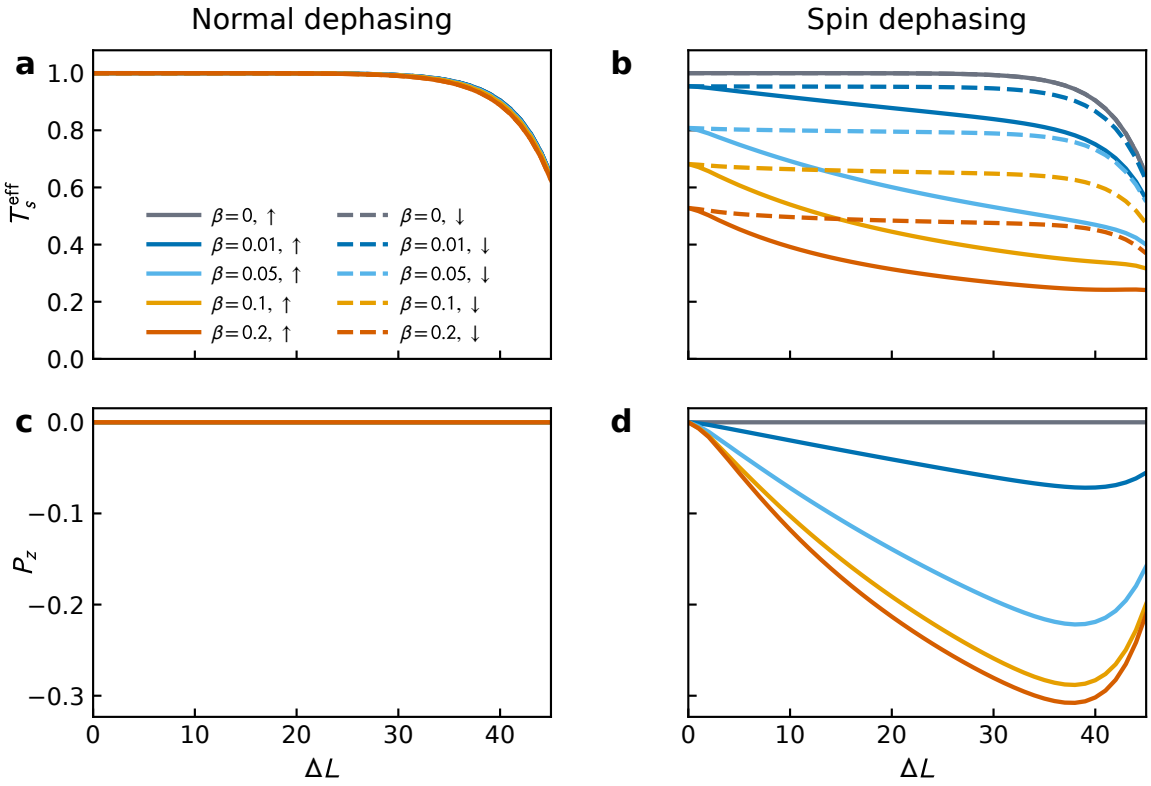

FIG. S6. Contact-length and dephasing-strength dependence of spin-selective tunneling in the QSH tip. (a,b) Spin-resolved effective transmissions $T^{\mathrm{eff}}_{R\uparrow\leftarrow L}$ (solid lines) and $T^{\mathrm{eff}}_{R\downarrow\leftarrow L}$ (dashed lines) as functions of the contact asymmetry $\Delta L = N_y - N_c$ for (a) normal dephasing and (b) spin dephasing. Different colors correspond to $\beta/t = 0$, 0.01, 0.05, 0.1, and 0.2. (c,d) Corresponding tunneling spin polarization P_s for (c) normal dephasing and (d) spin dephasing. Normal dephasing preserves equal spin transmissions and yields $P_s = 0$ for all contact lengths, whereas spin dephasing produces unequal transmissions and a finite negative polarization when $\Delta L \neq 0$. The polarization is nonmonotonic in ΔL, reflecting the competition between unequal spin-relaxing scattering along the helical paths and the reduced coupling associated with a short tunneling contact. The parameters are $E = 0.2t$, $N_y = 50$, $L_{\mathrm{QSH}} = 9$, $L_{\mathrm{NM}} = 2$, and $t_c = 0.6t$, with a uniform QSH on-site shift of $-0.01t$. The probe configuration is kept fixed throughout the contact-length scan.

B. Dependence on the tip–sample coupling strength

Figure S7 displays the total conductance and tunneling spin polarization for the QSH tip coupled to a spin-degenerate normal-metal sample. Over the coupling range $0.5 \leq t_c/t \leq 2$, both quantities exhibit only a weak dependence on the tip-sample coupling strength: the conductance varies moderately, while the spin polarization remains robustly negative with a nearly constant magnitude. This insensitivity to t_c indicates that the spin-selective tunneling response is highly stable against variations in the contact coupling within this regime.

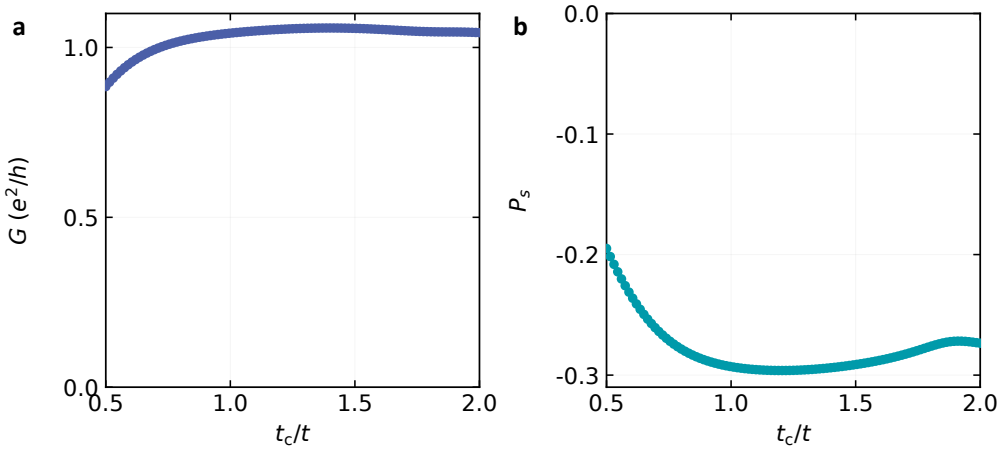

FIG. S7. Dependence on the tip–sample coupling strength of (a) the total conductance G and (b) the tunneling spin polarization P_s for a QSH tip coupled to a spin-degenerate normal-metal sample. Both quantities exhibit modest variations over $0.5 \leq t_c/t \leq 2$, with the polarization remaining negative. The parameters are $N_y = 40$, $L_{\mathrm{QSH}} = 9$, $L_{\mathrm{NM}} = 2$, $N_c = 10$, $E = 0.01t$, and $\beta = 0.1t$. Spin-dephasing probes occupy the outermost three layers along the upper, lower, and right boundaries of the QSH region.

S3. MAGNETIZATION-DEPENDENT CONDUCTANCE AND BIAS-INDUCED CONTRAST REVERSAL

We investigate the magnetization sensitivity of the asymmetric QSH tip by comparing its tunneling conductance for a uniformly magnetized ferromagnetic sample with opposite exchange fields, $M_{\mathrm{sample}} = \pm 0.5t$, as illustrated in Fig. S8(a,b). For several contact asymmetries ΔL, we calculate the conductances G_{+M} and G_{-M} as functions of the dephasing strength β and evaluate their normalized difference, the magnetization contrast $C_M = (G_{+M} - G_{-M})/(G_{+M} + G_{-M})$. Evidently, the contrast C_M increases with the sample exchange field M_{sample}.

As shown in Fig. S8(c,d), finite dephasing produces a conductance difference between the two magnetization orientations, and larger contact asymmetry enhances the contrast within the range considered. We also repeat the comparison under reversed bias for $\Delta L = 40$. The magnetization contrast changes sign upon bias reversal, again demonstrating its consistency with the experimental findings.

S4. RASHBA SPIN–ORBIT COUPLING AND THE CALCULATION OF MAIN TEXT FIG. 5

A. Rashba Hamiltonian and terminal conventions

The Rashba term is included throughout the finite QSH region and the semi-infinite left lead by the replacements

$$T_x \longmapsto T_x + \frac{i\alpha_R}{2}\sigma_y\tau_0, \quad T_y \longmapsto T_y - \frac{i\alpha_R}{2}\sigma_x\tau_0. \tag{S55}$$

With $c_{\boldsymbol{r}} = N^{-1/2}\sum_{\boldsymbol{k}} e^{i\boldsymbol{k}\cdot\boldsymbol{r}} c_{\boldsymbol{k}}$, these hopping blocks give

$$H_R(\boldsymbol{k}) = \alpha_R(\sin k_x\, \sigma_y - \sin k_y\, \sigma_x)\tau_0. \tag{S56}$$

The sample and the tunneling contact remain spin independent. For finite α_R, σ_z is not conserved in the QSH tip, so the Γ_α can not be decomposed into $\Gamma_{\alpha'\uparrow} + \Gamma_{\alpha'\downarrow}$, $\alpha' \in \{L, 1, \ldots, N\}$($R$ terminal is not affected), We therefore use the

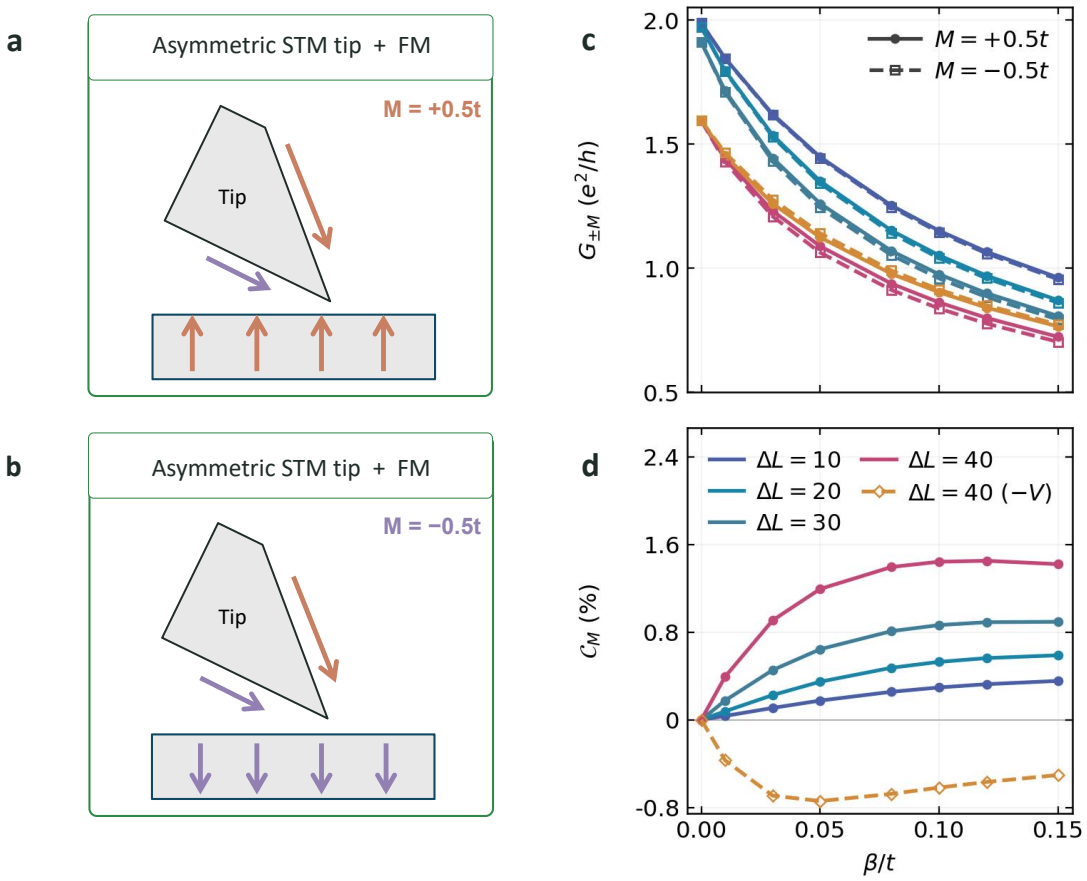

FIG. S8. Magnetization-sensitive tunneling with an asymmetric QSH tip. (a,b) Schematics for opposite sample exchange fields, $M_{\text{sample}} = +0.5t$ and $-0.5t$, respectively. (c) Corresponding conductances G_{+M} (solid lines with filled circles) and G_{-M} (dashed lines with open squares) versus the dephasing strength β. (d) Magnetization contrast $C_M = (G_{+M} - G_{-M})/(G_{+M} + G_{-M})$, expressed as a percentage. Different colors represent the contact asymmetries indicated in (d). Orange curves show the reversed-bias results for $\Delta L = 40$, for which the magnetization contrast reverses sign.

full broadening matrix $\Gamma_{\alpha'}$. As in the Rashba calculation of the main text, only spin dephasing is considered: the two spin components of each Büttiker probe share the voltage V_p, and $I_p = I_{p\uparrow} + I_{p\downarrow} = 0$. We write the probe broadening matrix:

$$\Gamma_p = \beta \sum_{\sigma} \Pi_{p\sigma} \tag{S57}$$

In this section, terminal indices $\sigma, \sigma' \in \{L, R, 1, \ldots, N\}$ label physical leads or Büttiker probes without an additional spin label, while the right lead is spin degenerate, so the outgoing spin components can still be resolved there.

B. Nonequilibrium density matrix approach and consistency with the main text

In the Sec. S1 E, we have introduced $\mathcal{T}_R(E) = G^r(E)\left[\Gamma_L(E) + \sum_p \frac{V_p}{V}\Gamma_p\right] G^a(E)$ and $\delta\rho(E) = \frac{eV}{2\pi}\mathcal{T}_R(E)$. Thus $\mathcal{T}_R$ is the effective transmission matrix defined in the main text. Following the definition in the main text, we have $X_R(E) = \Gamma_R^{1/2}(E)\mathcal{T}_R(E)\Gamma_R^{1/2}(E)$, $\mathcal{S}(E) = \mathrm{Tr}'\, X_R(E)$, and $P_i(E) = \mathrm{Tr}[\sigma_i \mathcal{S}(E)]/\,\mathrm{Tr}[\mathcal{S}(E)]$, $i = x, y, z$. This is the transmitted-spin density-matrix construction [11]. Each injecting terminal contributes the positive-semidefinite matrix

$$X_R^{(\alpha')} = \Gamma_R^{1/2} G^r \Gamma_{\alpha'} G^a \Gamma_R^{1/2} \tag{S58}$$

where $\mathrm{Tr}\, X_R^{(\alpha')} = T_{R\leftarrow\alpha'}$. With weight 1 for the left lead and V_p/V for probe p. Consequently,

$$\mathrm{Tr}\,\mathcal{S} = T_{R\leftarrow L} + \sum_p \frac{V_p}{V} T_{R\leftarrow p} = T^{\mathrm{eff}}_{R\leftarrow L}, \qquad I_R = \frac{e^2 V}{h} T^{\mathrm{eff}}_{R\leftarrow L}. \tag{S59}$$

which is consistent with our definition without Rashba SOC.

C. Mode-resolved coherent scattering states and local spin polarization

Main text Fig. 4(c,d) resolves the upper-edge and lower-edge contributions by injecting one right-moving helical mode at a time in the coherent limit, $\beta = 0$. The incoming Bloch wave is an asymptotic lead state; its continuation through the finite central scattering region must be obtained by imposing the outgoing boundary conditions in both leads. The following derivation makes the incident wave, the cut-lead resolvents, and the resulting source vector explicit, following the mode-matching construction [10].

1. Incoming Bloch mode and unit-flux normalization

In the following text, a superscript R on a quantity denotes the presence of Rashba SOC. Let H_0^R and $H^R_{x+i,x}$ be the intra-slice block and the inter-slice hopping matrix from x slice to $x+i$ slice of the uniform left lead with Rashba SOC, which reduces to H_0 and H_x in the absence of Rashba SOC. So the Eq.S36 should be written as:

$\mathrm{H}^R_{\mathrm{QSH}}(k_x) = H_0^R + H^R_{x,x-1}e^{-ik_x} + H^R_{x,x+1}e^{ik_x}$.(S60) The full Hamiltonian $H^R_{\mathrm{QSH}}(k_x)$ describes the doubly infinite uniform ribbon, whose eigenstates are the Bloch sequence. Each slice has $4N_y$ components. Given a k_n, an incoming mode n at energy E is selected by

$$H^R_{\mathrm{QSH}}(k_n)u_n = Eu_n, \qquad u_n^\dagger u_n = 1 \tag{S61}$$

We select this mode with the condition of $v_n = u_n^\dagger\, \partial_{k_x} H^R_{\mathrm{QSH}}(k_x)\big|_{k_n} u_n > 0$ for picking up the right-moving modes ,and also we need the factor $1/\sqrt{v_n}$ gives unit incident particle flux [10, 12]. We define $\phi_{n,0} = \frac{u_n}{\sqrt{v_n}}$ on $x = 0$ slice,which also satisfies the plane-wave mode:$\phi_{n,x} = e^{ik_n x}\phi_{n,0}$. The $4N_y$-component vector $\phi_{n,0}$ includes all transverse sites and four internal amplitudes per site. Upper- and lower-edge modes are distinguished by their transverse localization.

2. Residual of the incoming wave on the cut left lead

The Bloch sequence solves the Schrödinger equation of the doubly infinite uniform ribbon. In contrast, $H^{R,\mathrm{cut}}_{\mathrm{QSH}}$ acts only on $x \le -1$ and omits the bond between -1 and 0. Restrict the incoming sequence to this half-line:

$$(\Phi_n^{\mathrm{in}})_x = e^{ik_n x}\phi_{n,0}, \qquad x \le -1. \tag{S62}$$

At interior slices, both longitudinal neighbors remain in the cut lead, so

$$\left[(E - H^{R,\mathrm{cut}}_{\mathrm{QSH}})\Phi_n^{\mathrm{in}}\right]_x = 0, \qquad x \le -2. \tag{S63}$$

Here, the subscript x extracts the block corresponding to the x slice, rather than a single matrix element. At the surface slice, the uncut Bloch equation reads

$$E\phi_{n,-1} = H_0^R\phi_{n,-1} + H^R_{-1,-2}\phi_{n,-2} + H^R_{-1,0}\phi_{n,0}. \tag{S64}$$

The cut Hamiltonian retains only the first two terms on the right. Subtracting its action therefore leaves

$$\left[(E - H^{R,\mathrm{cut}}_{\mathrm{QSH}})\Phi_n^{\mathrm{in}}\right]_{x=-1} = (E - H_0^R)\phi_{n,-1} - H^R_{-1,-2}\phi_{n,-2} = H^R_{-1,0}\phi_{n,0}. \tag{S65}$$

Combining the interior and surface equations gives the complete cut-lead residual:

$$\left[(E - H^{R,\mathrm{cut}}_{\mathrm{QSH}})\Phi_n^{\mathrm{in}}\right]_x = \delta_{x,-1}H^R_{-1,0}\phi_{n,0}, \qquad x \le -1. \tag{S66}$$

This residual is the contribution of the deleted interface bond. It is nonzero only at the lead surface and must be retained when the incoming wave is matched to the central region.

3. Outgoing corrections and elimination of the two leads

Following the longitudinal indexing of the main text, the central region occupies $0 \le x \le x_{\rm c}$, where $x_{\rm c} = L_{\rm QSH} + L_{\rm NM}$; the right lead begins at $x_{\rm c}+1$. Write the n-th scattering state as $\Psi_n = (\psi_{L,n}, \psi_{C,n}, \psi_{R,n})^T$, we have the complete Schrödinger equation:

$$\begin{pmatrix} E - H_{\rm QSH}^{R,\rm cut} & -H_{-1,0}^{R} & 0 \\ -H_{0,-1}^{R} & E - H_C^R & -H'^{R}_{x_c,x_c+1} \\ 0 & -H'^{R}_{x_c+1,x_c} & E - H_{NM}^R \end{pmatrix} \begin{pmatrix} \psi_{L,n} \\ \psi_{C,n} \\ \psi_{R,n} \end{pmatrix} = \begin{pmatrix} 0 \\ 0 \\ 0 \end{pmatrix} \tag{S67}$$

Here, $H'^{R}_{x+i,x}$ refers to longitudinal hopping matrix from x slice block to $x+i$ slice block in NM lead with Rashba SOC, and H_{NM}^R represents the semi-infinite NM lead hamitonian with Rashba SOC. H_C^R denotes H_C in the presence of Rashba SOC.

In the left lead, the Schrödinger equation is

$$\Big[(E - H_{\rm QSH}^{R,\rm cut})\psi_{L,n}\Big]_x = \delta_{x,-1} H_{-1,0}^{R} [\psi_{C,n}]_{x=0}. \tag{S68}$$

Separate the prescribed incoming wave from the outgoing correction, $\psi_{L,n} = \Phi_n^{\rm in} + \chi_{L,n}$. Subtracting Eq. (S66) yields

$$\Big[(E - H_{\rm QSH}^{R,cut})\chi_{L,n}\Big]_x = \delta_{x,-1} H_{-1,0}^{R} ([\psi_{C,n}]_{x=0} - \phi_{n,0}). \tag{S69}$$

Applying the retarded resolvent gives the outgoing or decaying response. Its surface amplitude is

$$[\psi_{L,n}]_{x=-1} = \phi_{n,-1} + g_L^{r,R} H_{-1,0}^{R} ([\psi_{C,n}]_{x=0} - \phi_{n,0}). \tag{S70}$$

$g_L^{r,R}$ is the left-lead surface Green function with Rashba SOC, same as $g_R^{r,R}$. Furthermore, third row of Eq.S67 gives us the Schrödinger equation on the right-lead side:

$$[\psi_{R,n}]_{x=x_{\rm c}+1} = g_R^{r,R} H'^{R}_{x_{\rm c}+1,x_{\rm c}} [\psi_{C,n}]_{x=x_{\rm c}}. \tag{S71}$$

It is useful to distinguish the surface self-energy blocks from their embedding in the full central Hilbert space:

$$\Sigma_L^{r,R}(E) = \begin{bmatrix} H_{0,-1}^{R} g_L^{r,R}(E) H_{-1,0}^{R} & \cdots & 0 \\ \vdots & \ddots & \vdots \\ 0 & \cdots & 0 \end{bmatrix}, \quad \Sigma_R^{r,R}(E) = \begin{bmatrix} 0 & \cdots & 0 \\ \vdots & \ddots & \vdots \\ 0 & \cdots & H'^{R}_{x_c,x_c+1} g_R^{r,R}(E) H'^{R}_{x_c+1,x_c} \end{bmatrix}. \tag{S72}$$

The first matrix $\Sigma_L^{r,R}(E)$ is $4S \times 4S$ and its nonzero portion is $4N_y \times 4N_y$ acting on the $x=0$ slice; whereas the second matrix $\Sigma_R^{r,R}(E)$ is $4S \times 4S$ with its nonzero portion is $4N_y \times 4N_y$ acting on the $x = x_c$ slice . Before eliminating the leads, the second row of Eq.S67 has boundary terms

$$\big[(E - H_C^R)\psi_{C,n}\big]_x = \delta_{x,0} H_{0,-1}^{R} [\psi_{L,n}]_{x=-1} + \delta_{x,x_{\rm c}} H'^{R}_{x_{\rm c},x_{\rm c}+1} [\psi_{R,n}]_{x=x_{\rm c}+1}. \tag{S73}$$

Substituting Eq. (S70) and (S71) gives

$$\big[(E - H_C^R)\psi_{C,n}\big]_x = \begin{cases} H_{0,-1}^{R} e^{-ik_n}\phi_{n,0} + [\Sigma_L^{r,R}(E)]_{x=0}([\psi_{C,n}]_{x=0} - \phi_{n,0}), & x = 0, \\ 0, & 0 < x < x_{\rm c}, \\ [\Sigma_R^{r,R}(E)]_{x=x_c} [\psi_{C,n}]_{x=x_c}, & x = x_{\rm c}. \end{cases} \tag{S74}$$

Moving the terms proportional to the unknown boundary amplitudes to the left produces the finite scattering problem

$$\Big[E\mathbf{I} - H_C^R - \Sigma_L^{r,R} - \Sigma_R^{r,R}\Big]\psi_{C,n} = b_n, \qquad (b_n)_x = \begin{cases} \Big[H_{0,-1}^{R} e^{-ik_n} - [\Sigma_L^{r,R}(E)]_{x=0}\Big]\phi_{n,0}, & x = 0, \\ 0, & x \neq 0. \end{cases} \tag{S75}$$

Here, b_n has dimensions of $4S \times 1$, matching the dimensions of $\psi_{C,n}$. All retarded quantities are understood as their $E + i0^+$ boundary values. The phase e^{-ik_n} is the incoming Bloch phase on slice -1 relative to slice 0. The subtraction $-[\Sigma_L^{r,R}(E)]_{x=0}\phi_{n,0}$ follows from the cut-lead residual; omitting it changes the imposed boundary condition.

4. Finite linear solve and numerical conventions

The solution in the central region is

$$\psi_{C,n} = G^{r,R}(E) b_n. \tag{S76}$$

where $G^{r,R}(E) = \left[E\mathbf{I} - H_C^R - \Sigma_L^{r,R} - \Sigma_R^{r,R}\right]^{-1}$ with dimensions of $4S \times 4S$. Therefore, applying different chosen modes at fixed energy E to Eq.S76 gets corresponding $\psi_{C,n}$ in the central region[12]. The parameters of the mode-resolved maps are $\alpha_R = 0.30t$, $E = 0.01t$, $N_y = 50$, $N_c = 10$, $L_{\mathrm{QSH}} = 10$, and $L_{\mathrm{NM}} = 2$, with a uniform QSH on-site shift of $-0.01t$. The overall phase of $\psi_{C,n}$ follows the phase chosen for u_n and does not affect any local observable below.

D. Local spin polarization of a single scattering state

Let $[\psi_{C,n}]_{\boldsymbol{r}}$ denote the four-component block of $\psi_{C,n}$ at site $\boldsymbol{r} = (x, y)$. The local particle weight at this site is defined as

$$w_n(\boldsymbol{r}) = [\psi_{C,n}]_{\boldsymbol{r}}^{\dagger} [\psi_{C,n}]_{\boldsymbol{r}}, \tag{S77}$$

which represents the total probability density distributed over the four internal degrees of freedom at site $\boldsymbol{r}$.

The local spin polarization along the z-axis is then given by the expectation value of the spin operator,

$$P_z^{(n)}(\boldsymbol{r}) = \frac{[\psi_{C,n}]_{\boldsymbol{r}}^{\dagger} (\sigma_z \tau_0) [\psi_{C,n}]_{\boldsymbol{r}}}{w_n(\boldsymbol{r})}, \tag{S78}$$

Explicitly writing out the four components, the local spin polarization reads

$$P_z^{(n)}(\boldsymbol{r}) = \frac{|\psi_{n,1}|^2 + |\psi_{n,2}|^2 - |\psi_{n,3}|^2 - |\psi_{n,4}|^2}{|\psi_{n,1}|^2 + |\psi_{n,2}|^2 + |\psi_{n,3}|^2 + |\psi_{n,4}|^2}, \tag{S79}$$

which highlights the imbalance between the spin-up (components 1 and 2) and spin-down (components 3 and 4) weights at site $\boldsymbol{r}$.

[1] C. Caroli, R. Combescot, P. Nozières, and D. Saint-James, J. Phys. C **4**, 916 (1971).
[2] S. Datta, *Quantum Transport: Atom to Transistor* (Cambridge University Press, 2005).
[3] M. Büttiker, Phys. Rev. Lett. **57**, 1761 (1986).
[4] J. L. D'Amato and H. M. Pastawski, Phys. Rev. B **41**, 7411 (1990).
[5] H. Jiang, S. Cheng, Q.-f. Sun, and X. C. Xie, Phys. Rev. Lett. **103**, 036803 (2009).
[6] J. Bardeen, Phys. Rev. Lett. **6**, 57 (1961).
[7] D. Wortmann, H. Ishida, and S. Blügel, Phys. Rev. B **72**, 235113 (2005).
[8] A. Cresti, R. Farchioni, G. Grosso, and G. Pastori Parravicini, Keldysh-Green function formalism for current profiles in mesoscopic systems, Phys. Rev. B **68**, 075306 (2003). https://doi.org/10.1103/PhysRevB.68.075306.
[9] B. K. Nikolić, L. P. Zârbo, and S. Souma, Imaging mesoscopic spin Hall flow: Spatial distribution of local spin currents and spin densities in and out of multiterminal spin-orbit coupled semiconductor nanostructures, Phys. Rev. B **73**, 075303 (2006). https://doi.org/10.1103/PhysRevB.73.075303.
[10] P. A. Khomyakov, G. Brocks, V. Karpan, M. Zwierzycki, and P. J. Kelly, Conductance calculations for quantum wires and interfaces: Mode matching and Green's functions, Phys. Rev. B **72**, 035450 (2005). doi:10.1103/PhysRevB.72.035450.
[11] B. K. Nikolić and S. Souma, Decoherence of transported spin in multichannel spin-orbit-coupled spintronic devices: Scattering approach to spin-density matrix from the ballistic to the localized regime, Phys. Rev. B **71**, 195328 (2005). doi:10.1103/PhysRevB.71.195328.
[12] C. W. Groth, M. Wimmer, A. R. Akhmerov, and X. Waintal, Kwant: a software package for quantum transport, New J. Phys. **16**, 063065 (2014). doi:10.1088/1367-2630/16/6/063065.